Journal of Sound and Vibration (2002) **257**(5), 903–929
doi:10.1006/jsvi.5067, available online at http://www.idealibrary.com on IDEAL®

COUPLED TRANSVERSE AND AXIAL MOTION OF A COMPLIANT STRUCTURE IN RESPONSE TO VORTEX-SHEDDING LOADS

S. N. Kuchnicki and H. Benaroya

Mechanical and Aerospace Engineering, Rutgers, the State University of New Jersey, Piscataway, NJ 08854-8058, *U.S.A.*

(*Received* 21 *June* 2001, *and in final form* 15 *January* 2002)

A compliant offshore tower is modelled as a structure having extensional and transverse degrees of freedom. McIver's extension of Hamilton's principle is applied to the system, resulting in coupled non-linear equations of motion, due to the assumption of small strain and moderate rotation. The equations of motion are discretized using finite differences and solved numerically. Several forms for the vortex-shedding load are tested, as well as experimental force data. To better understand the model response, Monte Carlo simulations are performed. The results show the feasibility of the present model for representing the response of a compliant structure subject to transverse loading.

1. INTRODUCTION

The problem of vortex shedding from bluff bodies has been studied for over a century, reflected by the extensive literature on the subject. Many mathematical models for vortex-induced vibration exist in the literature, and are well enumerated in previous review papers on the subject. Some of the more recent of these include Sarpkaya [1], Bearman [2], Billah [3], and Kuchnicki [4]. This paper applies a novel approach to this century-old problem.

1.1. OFFSHORE STRUCTURES

Offshore structures are used for many purposes in the oil industry, including exploration, storage, and production. Two general types of offshore structures exist for these applications: Fixed structures, which resist wind, wave, and current forces with negligible displacement, and compliant structures, which experience small displacements that cannot be neglected. While the fixed structure has been a standard for many years in offshore applications, the need to exploit resources located in deeper water, combined with the bulkiness and impracticality of fixed structures in deep water applications, makes compliant structures an attractive and viable alternative.

An extensive review of the different types of compliant offshore structures is given by Adrezin *et al.* [5]. The major types are the articulated tower (Figure 1) and the tension leg platform (Figure 2). The articulated tower consists of a shaft holding several buoyancy and ballast chambers, attached to the ocean floor by a universal joint. The tension leg platform has a large ballast chamber secured to the ocean floor by four, eight, or more

0022-460X/02/$35.00

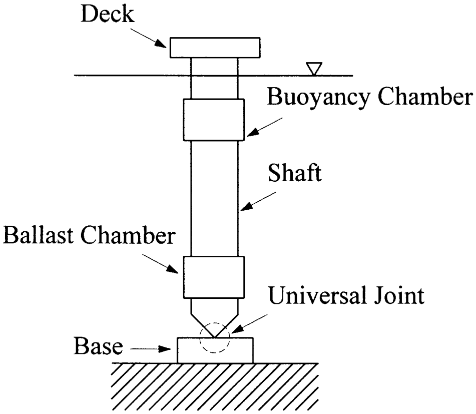

Figure 1. Schematic of a typical articulated tower.

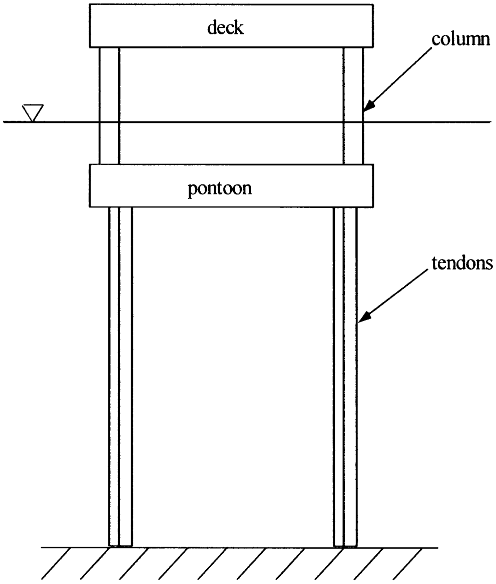

Figure 2. Typical tension leg platform.

tendons. In general, the vertical shaft of the articulated tower and the tendons of the tension leg platform can both be modelled as flexible beams.

A compliant structure undergoes loading due to wind and wave forces, as well as other forces due to shedding of vortices. Han and Benaroya [6, 7], examined the free response of such a structure, and its response to empirical (Morison) wave loads. This study looks at the third category, forces due to vortex-shedding loads. This work is in concert with an experimental effort by Dr Timothy Wei at Rutgers University, and so the system examined is related as closely as possible to the experimental set-up. In particular, the cylinder properties and torsional spring constant are from the experimental set-up. Also, since the experiment is constrained to transverse motion (there is no streamwise deflection allowed), our formulation omits streamwise deflection.

2. MCIVER'S EXTENSION

Before we derive the equations of motion for our system, a brief review of McIver's pioneering work is warranted. McIver [8] coupled Reynolds' transport theorem and Hamilton's principle. The result is a new theory that allows Hamilton's principle to be applied to fluid–structure systems using a control volume approach.[†] We briefly introduce McIver's work here; further detail can be found in references [8, 9, 4]. This work is a continuation of Benaroya and Wei [9]. McIver's extension begins with d'Alembert's principle for a continuous system

$$\delta \mathscr{L} + \delta W - \frac{\mathrm{d}}{\mathrm{d}t}\int_{v} (\rho \mathbf{U})\cdot\delta\mathbf{r} = 0, \tag{1}$$

where $\delta\mathbf{r}$ is a vector of virtual displacements, with one component for each degree of freedom of the system, and v is the volume of the system. Reynolds' transport theorem states:

$$\frac{\mathrm{d}}{\mathrm{d}t}\int_{system} (\rho \mathscr{Q})\,\mathrm{d}v = \int_{CV} \frac{\partial}{\partial t}(\rho \mathscr{Q})\,\mathrm{d}v + \int_{CS} (\rho \mathscr{Q})\mathbf{U}\cdot\mathbf{n}\,\mathrm{d}s. \tag{2}$$

Here, $\mathscr{Q}$ represents the property of interest per unit mass (intensive property), ρ is the fluid density, $\mathbf{U}(\mathbf{x}, t)$ is the fluid velocity at any point on the control surface, and $\mathbf{n}(\mathbf{x})$ is an outward normal vector of the control surface.[‡] This relation is a statement that the rate of change of $\mathscr{Q}$ in the system is equal to the rate of change of $\mathscr{Q}$ within the control volume plus the net flux of $\mathscr{Q}$ across the control surface. If our property of interest is $\mathbf{U}\cdot\delta\mathbf{r}$, then the integral on the left-hand side of equation (2) is identical to the integral in equation (1).

Substitution gives the relation

$$\delta \mathscr{L}_{system} + \delta W - \int_{CV} \frac{\partial}{\partial t}(\rho \mathbf{U})\cdot\delta\mathbf{r}\,\mathrm{d}v - \int_{CS} (\rho \mathbf{U})\cdot\delta\mathbf{r}(\mathbf{U} - \mathbf{V}_{control})\cdot\mathbf{n}\,\mathrm{d}s = 0, \tag{3}$$

where the mass of the system in the Lagrangian ($\mathscr{L}_{system}$) is not fixed. Integrating equation (3) between the times t_1 and t_2, requiring the variations at the end times to be zero (eliminating the volume integral), leads us to the following restatement of Hamilton's principle:

$$\delta\int_{t_1}^{t_2} \mathscr{L}_{system}\,\mathrm{d}t + \int_{t_1}^{t_2} \delta W\,\mathrm{d}t - \int_{t_1}^{t_2}\int_{CS} (\rho \mathbf{U})\cdot\delta\mathbf{r}(\mathbf{U} - \mathbf{V}_{control})\cdot\mathbf{n}\,\mathrm{d}s\,\mathrm{d}t = 0. \tag{4}$$

The virtual work of the system is due to all non-potential forces acting on the system, including those due to surface tractions on the control surfaces. Specifically, these surface tractions are expressed as

$$\delta W = \int_{open\ CS} (-p\mathbf{n} + \tau_0)\cdot\delta\mathbf{r}\,\mathrm{d}s + \int_{closed\ CS} (-p\mathbf{n} + \tau_c)\cdot\delta\mathbf{r}\,\mathrm{d}s, \tag{5}$$

where $-p\mathbf{n}$ is the inward normal pressure on the control surface, τ_0 is the shear stress on the open control surface, and τ_c is the shear stress on the inner control surface.

The forcing functions used later in this paper will be assumed to include the fluid portions of the Lagrangian as well as these surface tractions.

[†] Normally, Hamilton's principle is only applicable to systems described as collections of particles.

[‡] The subscripts CV and CS refer to integrals over the control volume and control surface respectively.

3. ASSUMPTIONS AND FORMULATION

One of the advantages of the derivation above is that it is applicable to a general system Lagrangian. To derive the Lagrangian for the work at hand, we consider a beam of length L in the undeformed state. Elements of the beam are located by their location in the undeformed state, X. The midplane for the reference (undeformed) and current (deformed) configurations is given in Figure 3.

Applying Kirchhoff's hypothesis, we write the displacements as

$$u_1(X, Y, t) = u(X, t) - Y\frac{\partial}{\partial X}[v(X, t)],$$
$$u_2(X, t) = v(X, t), \qquad u_3(X, t) = 0, \tag{6}$$

where $u(X, t)$ is the deflection of the midplane in the x direction, and $v(X, t)$ is the deflection in the y direction. The co-ordinate Y is the distance from the midplane to the point of interest in the reference configuration. If we have a symmetrical cross-section, $u(X, t)$ is also the average deflection of the beam element at X. We assume small strains and moderate rotation. Mathematically, the consequences are

$$\frac{\partial u_1}{\partial X} \sim \left(\frac{\partial u_2}{\partial X}\right)^2 \ll 1, \tag{7}$$

or in terms of the midplane deflections,

$$\frac{\partial u}{\partial X} \sim \left(\frac{\partial v}{\partial X}\right)^2 \ll 1. \tag{8}$$

The conditions under which Kirchhoff's hypothesis is valid are that the strains are small compared to the rotation. Thus, equation (8) is a formal mathematical statement of the implicit assumptions we made to arrive at our displacement field.

Applying the assumption of small strain and moderate rotation, we get the Green strains:

$$\mathscr{E}_{XX} = \frac{\partial u_1}{\partial X} + \frac{1}{2}\left(\frac{\partial u_2}{\partial X}\right)^2, \qquad \mathscr{E}_{YY} = \frac{\partial u_2}{\partial Y}, \qquad \mathscr{E}_{ZZ} = 0,$$
$$\mathscr{E}_{XY} = \frac{1}{2}\left[\frac{\partial u_2}{\partial X} + \frac{\partial u_1}{\partial Y}\right], \qquad \mathscr{E}_{YZ} = 0, \qquad \mathscr{E}_{XZ} = 0. \tag{9}$$

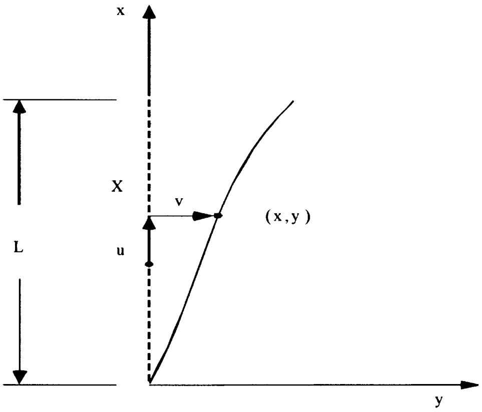

Figure 3. Midplane of the tower system in the original and deformed states.

Substituting our assumed displacement field into equation (6) gives the Green strains for our problem:

$$\mathscr{E}_{XX} = \frac{\partial u}{\partial X} - Y\frac{\partial^2 v}{\partial X^2} + \frac{1}{2}\left(\frac{\partial v}{\partial X}\right)^2, \qquad \mathscr{E}_{YY} = 0, \qquad \mathscr{E}_{XY} = 0. \tag{10}$$

If we ignore the Poisson effect, the second Kirchhoff stress is given by

$$\tilde{\sigma}_{XX} = E\mathscr{E}_{XX}, \tag{11}$$

where E is Young's modulus of the material in question.

4. ENERGIES AND THE LAGRANGIAN

Let us first examine the strain energy of the beam, given by

$$PE_{strain} = \frac{1}{2}\int_{V_0} \tilde{\sigma}_{ij}\mathscr{E}_{ij}\,\mathrm{d}V_0, \tag{12}$$

where V_0 is the volume of the undeformed beam. We substitute the expressions for the second Kirchhoff stress and the Green strain to obtain

$$PE_{strain} = \frac{1}{2}\int_X\int_{A_0}\left(u' - Yv'' + \frac{1}{2}v'^2\right)^2 \mathrm{d}A_0\,\mathrm{d}X, \tag{13}$$

where primes denote differentiation with respect to X and A_0 is the cross-sectional area in the undeformed state. We can expand the integrand to

$$\begin{aligned} PE_{strain} = &\frac{1}{2}\int_X\int_{A_0} E\big(u'^2 - 2Yu'v'' + u'v'^2 \\ &+ Y^2v''^2 - Yv'^2v'' + \frac{1}{4}v'^4\Big)\,\mathrm{d}A_0\,\mathrm{d}X. \end{aligned} \tag{14}$$

Since we have assumed a symmetric cross-section, integration over the entire area eliminates terms containing odd powers of Y, and turns terms containing Y^2 into terms with the area moment of inertia I_0 about the neutral axis. The remaining terms are functions of X and t.

The torsional spring has potential energy given by

$$PE_{spring} = \tfrac{1}{2}k\theta^2, \tag{15}$$

where θ is the angle of twist for the torsional spring. Assuming small angles, this angle can be expressed as the first spatial derivative of the transverse deflection at the base, or $v'(0,t)$.

Adding PE_{strain} to PE_{spring} gives the total potential energy of the system

$$PE = \frac{1}{2}\int_0^L\left[EA_0\left(u' + \frac{1}{2}v'^2\right)^2 + EI_0v''^2\right]\mathrm{d}X + \frac{1}{2}kv'^2(0,t). \tag{16}$$

The kinetic energy consists of the kinetic energy of the beam and the kinetic energy of the point mass. The kinetic energy of the beam is given as

$$KE_{beam} = \frac{1}{2}\int_0^L\int_{A_0}[\rho(\dot{u}_1^2 + \dot{u}_2^2)]\,\mathrm{d}A_0\,\mathrm{d}X, \tag{17}$$

where dots denote differentiation with respect to time. Substituting the displacement field from equation (6) leads to

$$\begin{aligned}KE_{beam} &= \frac{1}{2}\int_0^L\int_{A_0}[(\dot{u}-Y\dot{v}')^2+\dot{v}^2]\,\mathrm{d}A_0\,\mathrm{d}X\\ &= \frac{1}{2}\int_0^L\int_{A_0}(\dot{u}^2-2Y\dot{u}\dot{v}'+Y^2\dot{v}'^2+\dot{v}^2)\,\mathrm{d}A_0\,\mathrm{d}X\\ &= \frac{1}{2}\int_0^L[\rho A_0(\dot{u}^2+\dot{v}^2)+\rho I_0\dot{v}'^2]\,\mathrm{d}X, \end{aligned} \tag{18}$$

where we note again that since we have assumed a symmetric cross-section, odd powers of Y vanish when integrated over the entire area, and Y^2 becomes the area moment of inertia. The kinetic energy of the point mass is simply

$$KE_{mass} = \tfrac{1}{2}M_p[\dot{u}^2(L,t)+\dot{v}^2(L,t)]. \tag{19}$$

Adding equations (18) and (19) gives the total system kinetic energy

$$KE = \frac{1}{2}\int_0^L[\rho A_0(\dot{u}^2+\dot{v}^2)+\rho I_0\dot{v}'^2]\,\mathrm{d}X+\frac{1}{2}M_p[\dot{u}^2(L,t)+\dot{v}^2(L,t)]. \tag{20}$$

The term $\rho I_0\dot{v}'^2$ is Rayleigh's rotational term, or the kinetic energy due to the rotation of the cross-section. Even though this term is usually small in comparison to the translational kinetic energy of the beam, we will not ignore it for this analysis. Note also that we have made no statement about the density, area A_0 or area moment of inertia I_0. They can be constant or functions of X.

We wish to apply Hamilton's principle to the beam system. Thus, we first need the Lagrangian of the tower, defined as $\mathscr{L} = KE - PE$. Also, we define the forces acting on the system in the directions of u and v as $f_u(X,t)$ and $f_v(X,t)$ respectively.

5. HAMILTON'S PRINCIPLE

We state Hamilton's principle as

$$\delta\int_{t_1}^{t_2}\mathscr{L}_{structure}\,\mathrm{d}t+\int_{t_1}^{t_2}\delta H\,\mathrm{d}t = 0, \tag{21}$$

where the virtual work on the system, δH, is given by

$$\begin{aligned}\delta H &= \delta W+\int_{CS}(\rho\mathbf{U})\cdot\delta\mathbf{r}(\mathbf{U}-\mathbf{V}_{control})\cdot\mathbf{n}\,\mathrm{d}s\\ &= \int_0^L[f_u(X,t)\delta u+f_v(X,t)\delta v]\,\mathrm{d}X. \end{aligned} \tag{22}$$

Recall that δW was defined in equation (5). The force $f_u(X,t)$ is that due to gravity and buoyancy, and the force $f_v(X,t)$ is the transverse vortex-shedding load.

Let us concentrate on the Lagrangian portion of equation (21):

$$\begin{aligned}\delta\int_{t_1}^{t_2}\mathscr{L}_{structure}\,\mathrm{d}t = \int_{t_1}^{t_2}\int_0^L &\{[\rho A_0(\dot{u}\delta u+\dot{v}\delta v)+\rho I_0\dot{v}'\delta\dot{v}'\\ &-EA_0\left(u'+\frac{1}{2}v'^2\right)(\delta u'+v'\delta v')-EI_0v''\delta v''\Big]\,\mathrm{d}X\\ &+\ M_p[\dot{u}(L,t)\delta\dot{u}(L,t)+\dot{v}(L,t)\delta\dot{v}(L,t)]\\ &-kv'(0,t)\delta v'(0,t)\}\,\mathrm{d}t.\end{aligned}\tag{23}$$

We integrate individual terms by parts, with the goal of arriving at terms multiplied by δu and δv. This procedure results in

$$\begin{aligned}\delta\int_{t_1}^{t_2}\mathscr{L}\,\mathrm{d}t = \int_{t_1}^{t_2}\Bigg(&\int_0^L\left\{-\rho A_0\ddot{u}+\frac{\partial}{\partial X}\left[EA_0\left(u'+\frac{1}{2}v'^2\right)\right]\right\}\delta u\\ &+\left\{-\rho A_0\ddot{v}+\frac{\partial}{\partial X}\left[EA_0\left(u'+\frac{1}{2}v'^2\right)v'\right]\right.\\ &\left.+\rho I_0\ddot{v}''-\frac{\partial^2}{\partial X^2}(EI_0v'')\right\}\delta v\,\mathrm{d}X\Bigg)\,\mathrm{d}t\\ &+\int_{t_1}^{t_2}\left\{\left[\frac{\partial}{\partial X}(EI_0v'')-\rho I_0\ddot{v}'-EA_0\left(u'+\frac{1}{2}v'^2\right)v'\right]\delta v\right\}\Bigg|_{X=0}^{L}\,\mathrm{d}t\\ &+\int_{t_1}^{t_2}\left[-EA_0\left(u'+\frac{1}{2}v'^2\right)\delta u-EI_0v''\delta v'\right]\Bigg|_{X=0}^{L}\,\mathrm{d}t\\ &-\int_{t_1}^{t_2}M_p[\ddot{u}(L,t)\delta u(L,t)+\ddot{v}(L,t)\delta v(L,t)]\,\mathrm{d}t\\ &-\int_{t_1}^{t_2}kv'(0,t)\delta v'(0,t)\,\mathrm{d}t,\end{aligned}\tag{24}$$

where we note that the variation at the end times t_1 and t_2 are assumed zero, which results in the elimination of terms integrated by parts in time. Now, we apply Hamilton's principle as stated in equation (21) to get the equations of motion:

$$\begin{aligned}&\rho A_0\ddot{u}-\frac{\partial}{\partial X}\left[EA_0\left(u'+\frac{1}{2}v'^2\right)\right]=f_u,\\ &\rho A_0\ddot{v}-\frac{\partial}{\partial X}\left[EA_0\left(u'+\frac{1}{2}v'^2\right)v'\right]-\rho I_0\ddot{v}''+\frac{\partial^2}{\partial X^2}(EI_0v'')=f_v\end{aligned}\tag{25}$$

and the corresponding boundary conditions

$$\begin{aligned}&EA_0\left(u'+\frac{1}{2}v'^2\right)\delta u\Bigg|_{X=0}^{L}+M_p\ddot{u}(L,t)\delta u(L,t)=0,\\ &\left[\frac{\partial}{\partial X}(EI_0v'')-\rho I_0\ddot{v}'-EA_0\left(u'+\frac{1}{2}v'^2\right)v'\right]\delta v\Bigg|_{X=0}^{L}-M_p\ddot{v}(L,t)\delta v(L,t)=0,\\ &EI_0v''\delta v'|_{X=0}^{L}+kv'(0,t)\delta v'(0,t)=0.\end{aligned}\tag{26}$$

For the problem at hand, these boundary conditions become

$$u(0,t)=0,\qquad v(0,t)=0,\qquad v''(L,t)=0,\tag{27a−c}$$

$$kv'-EI_0v''|_{X=0,t}=0,\tag{27d}$$

$$EA_0\left(u' + \frac{1}{2}v'^2\right) + M_p\ddot{u}\bigg|_{X=L,t} = 0, \tag{27e}$$

$$\left[\frac{\partial}{\partial X}(EI_0v'') - \rho I_0\ddot{v}' - EA_0\left(u' + \frac{1}{2}v'^2\right)v'\right] - M_p\ddot{v}\bigg|_{X=L,t} = 0. \tag{27f}$$

6. NUMERICAL ISSUES AND DISCRETIZATION

6.1. DENSITY, AREA, AND AREA MOMENT OF INERTIA AS FUNCTIONS OF X

The actual tower has three types of sections: hollow (air-filled) acrylic, solid acrylic (where the plugs are located), and water-filled acrylic. Using the co-ordinates in the schematic, as well as the numbering conventions there, we arrive at relatively simple functions for the density, area, and area moment of inertia:

$$\rho(X) = \rho_1 + [\mathrm{H}(X - X_{3\mathrm{H}}) - \mathrm{H}(X - X_{3\mathrm{H}})](\rho_3 - \rho_1), \tag{28}$$

$$\begin{aligned} A_0(X) = A_1 + [&\mathrm{H}(X - X_{1L}) - \mathrm{H}(X - X_{1\mathrm{H}}) \\ &+ \mathrm{H}(X - X_{2L}) - \mathrm{H}(X - X_{3\mathrm{H}})](A_2 - A_1), \end{aligned} \tag{29}$$

$$\begin{aligned} I_0(X) = I_1 + [&\mathrm{H}(X - X_{1L}) - \mathrm{H}(X - X_{1\mathrm{H}}) \\ &+ \mathrm{H}(X - X_{2L}) - \mathrm{H}(X - X_{3\mathrm{H}})](I_2 - I_1), \end{aligned} \tag{30}$$

where $\mathrm{H}(X)$ is the Heaviside function, defined by

$$\mathrm{H}(X) = \begin{cases} 0 & X < 0, \\ 1 & X \geqslant 0. \end{cases} \tag{31}$$

Note that the derivative with respect to X of $\mathrm{H}(X)$ is the Dirac delta function, $\delta(X)$, and the second derivative of the Heaviside function is the Dirac doublet function. If we discretize the tower in such a way as to avoid the actual points of discontinuity ($X_{1L}, X_{1\mathrm{H}}$, etc.) then the derivatives of these tower properties with respect to X will be zero.

As a first approximation, we ignore these discontinuities in the tower properties. In practice, their inclusion makes the equations of motion stiff. These stiff equations proved difficult to solve for any useful time period, even when specialized solution routines for stiff equations were used.

6.2. FINITE DIFFERENCES AND BOUNDARY CONDITIONS

To analyze the tower motion, using MATLAB, we discretize it into N nodes. We represent spatial derivatives using central difference operators, as explained by previous authors [10, 4]. In order to use this method, we need to use the boundary conditions to find the displacements at several "dummy nodes," having indices -1, 0, $N+1$, and $N+2$. The boundary conditions will provide us with equations for displacements u_1, u_{N+1}, v_0, v_1, v_{N+1}, and v_{N+2}, where u_r represents the displacement u at node r.

Looking at the first two boundary conditions (equations (27a) and (27b)), we arrive at the relations

$$u_1 = 0, \qquad v_1 = 0. \tag{32}$$

Note that, from the definition of the central difference operators, v_{-1} is only needed to find v_1''' and v_1''''. Since we have the constraint $v_1 = 0$, we do not evaluate the equation for

v_1, and thus do not need v_{-1}. Continuing on to the boundary condition for the moment at the top of the beam in equation (27c), we find

$$v_{N+1} = 2v_N - v_{N-1}. \tag{33}$$

We next evaluate the boundary condition balancing the moment at the bottom with the spring moment (equation (27d)). Keeping in mind the constraint $v_1 = 0$, we arrive at

$$v_0 = \frac{kh - 2EI_0}{kh + 2EI_0} v_2, \tag{34}$$

where h is the spacing between nodes. Next, we evaluate u_{N+1} from the vertical force boundary condition at the top end (equation (27e)):

$$u_{N+1} = u_{N-1} - \frac{1}{h}[v_N - v_{N-1}]^2 - \frac{2hM_p}{EA_0}\ddot{u}_N. \tag{35}$$

This equation will provide us with some coupling between second derivatives of u and v near the top of the tower. Finally, we get v_{N+2} from equation (27f), noting that we can solve equation (27e) for $EA_0(u' + \frac{1}{2}v'^2)$:

$$\begin{aligned} v_{N+2} = {} & 4[v_N - v_{N-1}] + v_{N-2} + \frac{2h^2}{E}\left(\rho + \frac{M_p h}{I_0}\right)\ddot{v}_N \\ & - \frac{2\rho h^2}{E}\ddot{v}_{N-1} - \frac{2h^2 M_p}{EI_0}[v_N - v_{N-1}]\ddot{u}_N. \end{aligned} \tag{36}$$

This last equation more explicitly provides coupling between several accelerations of u and v at the top of the tower.

We can use the above relations plus the finite difference operators to construct a set of $2N$ equations of motion for the displacements u and v at the N nodes. The order of error is equal to h^2, the square of the spacing between nodes.

6.3. THE "SMALL STRAIN" ASSUMPTION

We made use of Kirchhoff's hypothesis in the derivation for the two-degree-of-freedom equations, which is valid only for small strains. This means that we need to check the results of the MATLAB simulations to see if our strains lie within the elastic region. The tower material is acrylic (polymethylmethacrylate, or PMMA), with Young's modulus of 3·174 GPa and flexural strength 131 MPa. This means that the tower can experience up to about 4% strain and remain within the elastic region.

The question is then, how do we find the strain, given the displacement field? There are two methods, the first of which serves as a quick calculation, and the second as the more exact method. To get a quick idea, we can look at the transverse displacement of the second node, and treat that as being completely due to rigid-body motion. Dividing this displacement by the spacing between nodes gives the tangent of the rigid-body rotation angle, which is then used to find the rigid-body displacement and strain at the top node. Of course, this method suffers from a flaw, specifically that some of the transverse deflection of node two may be (and likely is) due to deflection, so the angle found via this procedure is only an estimate.

To find the angle more exactly, we invoke equation (27d), with the substitution $v'(0, t) = \theta(t)$. Solving for $\theta(t)$ gives

$$\theta(t) = \frac{EI_0}{k} v''(0, t). \tag{37}$$

We can take this further, however, using the finite difference relations, since

$$v''(0,t) = v_1''(t) = \frac{v_2(t) - 2v_1(t) + v_0(t)}{h^2}. \tag{38}$$

Recall that $v_1(t) = 0$ by constraint, and that we have an expression for $v_0(t)$ from equation (34). We can then restate equation (37) as

$$\theta(t) = \frac{EI_0}{kh^2}\left[1 + \frac{kh - 2EI_0}{kh + 2EI_0}\right] v_2(t). \tag{39}$$

For the system in question, $k = 9{\cdot}7098$ N m/rad, $E = 3{\cdot}174$ GPa, $I_0 = 8{\cdot}509 \times 10^{-9}$ m^4, $h = 0{\cdot}0658$ m. So the factor multiplying $v_2(t)$ is 15·02 for the results that follow.

7. RESULTS AND DISCUSSION

7.1. TOWER SPECIFICS AND FORCING

Table 1 lists the properties for the tower used here. As mentioned above, we ignore the changes in tower properties caused by the plugs and water within the tower.

Since we are dealing with a discretized system of 20 nodes, we apply transverse forces to the nodes that are below the waterline only. The same is done with the vertical buoyancy force; it is applied solely to the nodes below the mean-water level. We also applied equal forces to each node, which implicitly ignores three-dimensional effects.

The form chosen for the vortex-shedding load is sinusoidal. We chose this form because the data from Dr Timothy Wei's experimental set-up at Rutgers University (upon which this system is based) showed both a sinusoidal cylinder motion and sinusoidal energy inputs, especially for the work done by pressure forces.

We tried several different sinusoidal forms for the vortex-shedding load. We varied amplitudes and frequencies, and finally settled on a Fourier-series formulation that contained as many as 50 frequencies, to try and include some of the high-frequency energy inputs observed in the water-tunnel experiments.

7.2. RESULTS

We began with a simple forcing function, $F_0 = 0{\cdot}002\sin(10t)$, with zero initial displacement and velocity. (Note that F_0 is the force applied to each node.) The results are plotted in Figures 4 and 5. The time scale of Figure 4 is too short to show the details of

Table 1

Cylinder properties

Property	Value
Young's modulus, E	3·174 GPa
Cross-sectional area, A_0	$1{\cdot}196 \times 10^{-4}$ m^2
Area moment of inertia, I_0	$8{\cdot}509 \times 10^{-9}$ m^4
Torsional spring stiffness, k	9·7098 N m/rad
Tower length, L	1·2509 m
Water depth, d	1·0668 m
End mass, M_p	0·1533 kg
Tower density, ρ	1136 kg/m^3
Number of nodes, N	20
Node spacing, h	0·0658 m

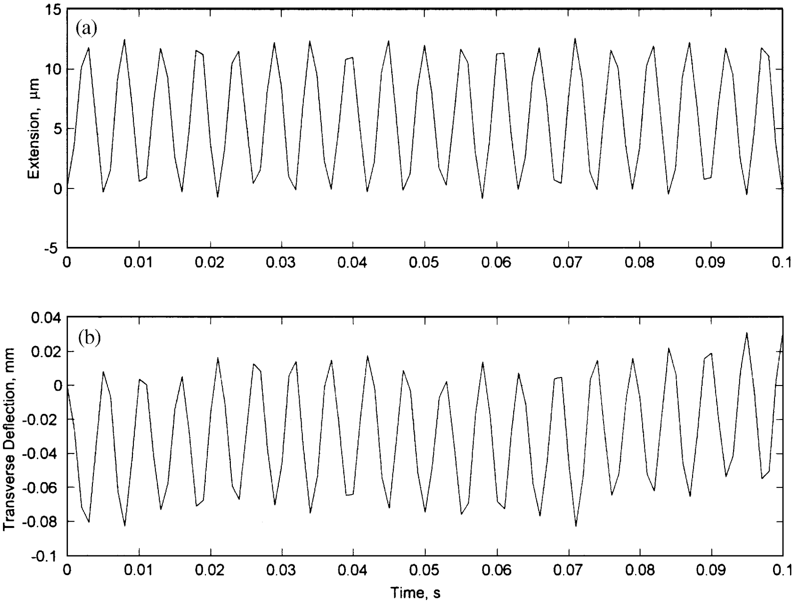

Figure 4. (a) Extensional and (b) transverse responses to $F_0 = 0{\cdot}002 \sin 10t$ for 0·1 s.

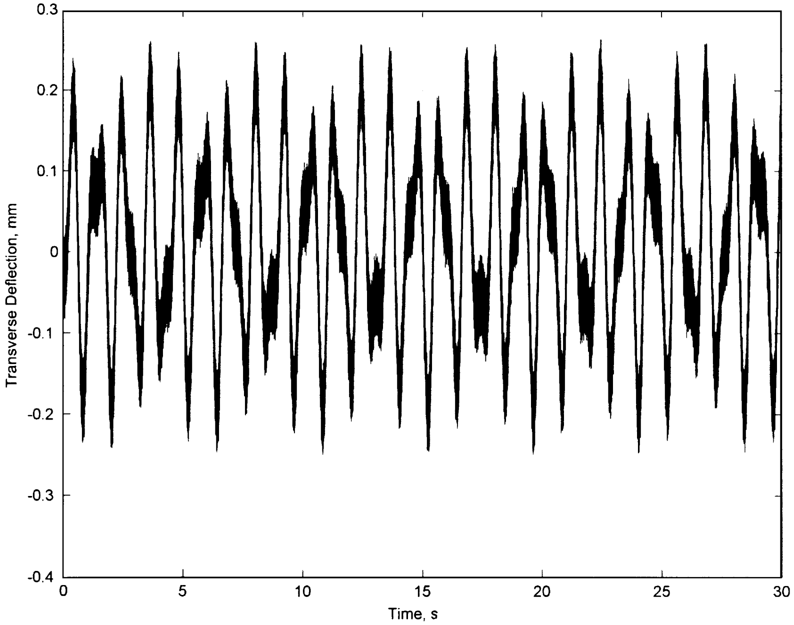

Figure 5. Transverse response to $F_0 = 0{\cdot}002 \sin 10t$ for a 30-s time period.

the high-frequency extensional motion and its coupling to the transverse motion. The high-frequency extension is expected since only gravity and buoyancy act in the longitudinal direction of the tower. As shown, the maximum amplitude is around 15 μm. The extensional behavior is the same for all parameter runs in this study, and is omitted from the remaining plots for brevity. The transverse deflection, shown for 30 s in Figure 5 shows oscillatory behavior at several frequencies, of which one is due to coupling with the extensional motion, one due to forcing, and the rest from the natural frequencies of the structure. Also, the maximum strain is calculated as 2·8%. To illustrate the distribution of energy, we plot a power spectral density of the transverse response in Figure 6.

Note that the frequencies are normalized to the Nyquist frequency, which is equal to 500 Hz, or about 3100 rad/s, for the responses given in this paper. By itself, this spectrum tells us that the tower has oscillation frequency components at many frequencies, with most of the energy contained in frequencies less than about 20 Hz, and the presence of some harmonics. There is an exception to this rule, and that occurs at about 190 Hz. The first thought upon seeing this spike is that it is likely to be due to the coupling between the transverse and extensional motion, or in other words, that this frequency corresponds to the frequency of the extensional oscillation. The power spectrum for the extensional motion, given in Figure 7, confirms this suspicion, as the plot shows a prominent peak in the same frequency range (about 190 Hz).

This spectrum also shows a harmonic at around 260 Hz, which is reflected in the transverse power spectrum. Also note the scale on both plots; the peaks in question are about the same magnitude on both plots as well. The very high frequency energies can be considered noise, as their magnitude is relatively small as well.

Our next example has changed the forcing to $F_0 = 0{\cdot}002\sin(t) + 0{\cdot}001\cos(t)$, while retaining zero initial conditions. The lower forcing frequency has caused a qualitative change in the response, while leaving the maximum amplitude relatively unchanged, as shown in Figure 8. The transverse response looks like a sum of two sinusoids of different frequency (ignoring the high-frequency contribution from the coupling to extensional motion), even though the forcing consists of two sinusoids of identical frequency. This

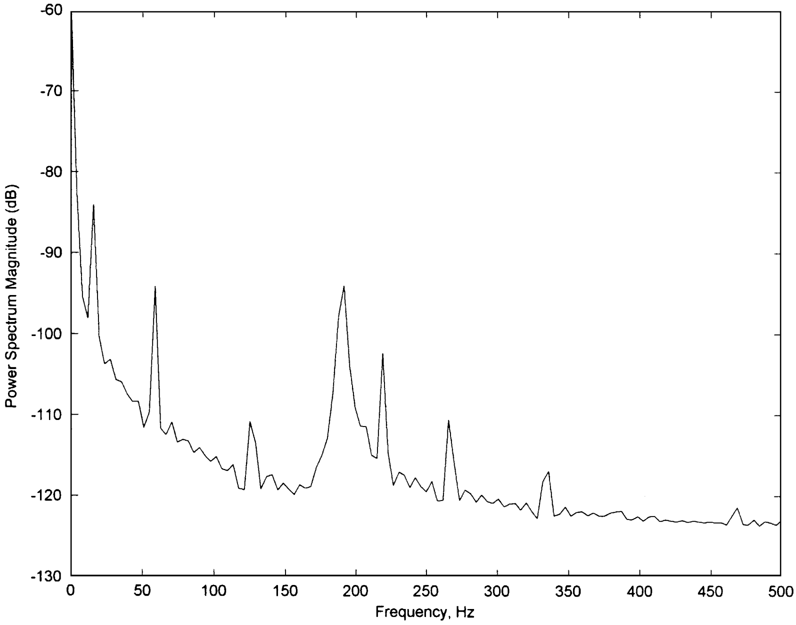

Figure 6. Power spectrum for the transverse response to $F_0 = 0{\cdot}002\sin 10t$.

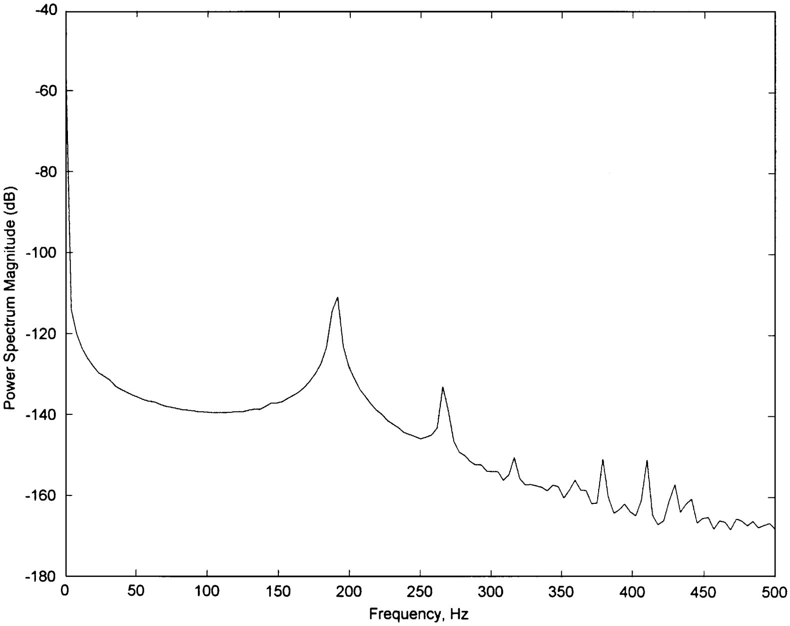

Figure 7. Power spectrum for the extensional response. Note the peak at 190 Hz.

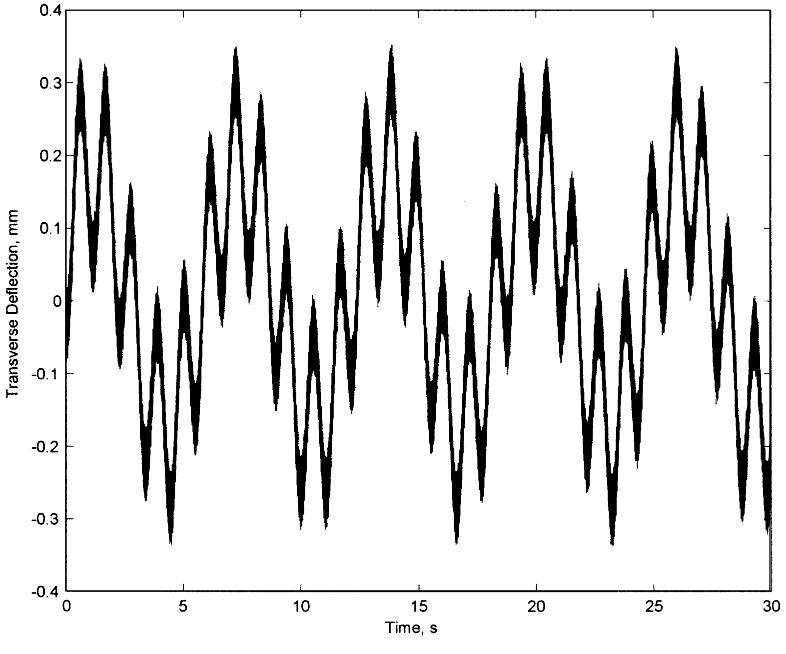

Figure 8. Responses to $F_0 = 0{\cdot}002\sin(t) + 0{\cdot}001\cos(t)$.

qualitative result highlights the non-linear character of the system. The maximum strain here was found to be 2·82%.

The power spectrum for the transverse response in this case (Figure 9) looks remarkably similar to the spectrum for the previous case. We have a large amount of energy in the low

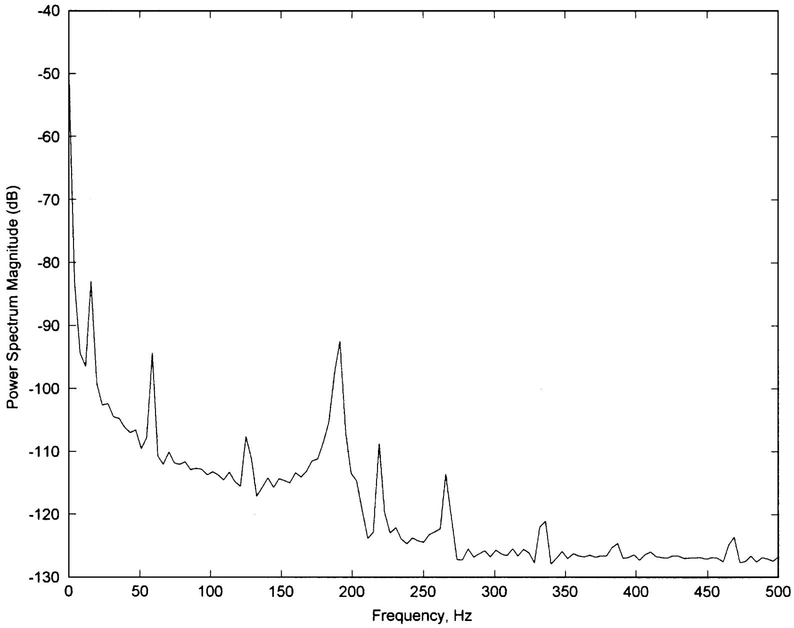

Figure 9. Power spectrum for the transverse response to $F_0 = 0{\cdot}002\sin(t) + 0{\cdot}001\cos(t)$.

frequencies, along with the double peak around the extensional oscillation frequency and its harmonic.

The next example uses $F_0 = 0{\cdot}003(\sin(5t) - \cos(t))$, retaining the same initial conditions. The transverse response, as presented in Figure 10 is again quite different than the previous cases, but retains its oscillatory character. The maximum amplitude and maximum strain have diminished from the previous examples, with the strain at a value of 1·65%. The response shows some characteristics similar to beating. The power spectrum for this case is similar to the previous two, and is not given here for brevity.

Our final example response with zero initial conditions involves a Fourier series as the input. We applied the sequence

$$F_0 = \frac{0{\cdot}003}{\sqrt{2}} + \frac{0{\cdot}001}{50}\sum_{n=0}^{50}\cos(n^2 t), \tag{40}$$

where the amplitudes are chosen to give a force amplitude comparable to the previous simulations, and the frequency range is chosen to be broad, giving a wide input spectrum, plotted in Figure 11. Note the broad band of frequencies provided as inputs.

The response to the Fourier input is presented in Figure 12. Note that the transverse response magnitude is relatively unchanged, while the transverse response form is more explicitly periodic than in previous responses. Also, the response shows some slight variation in amplitude, perhaps due to another appearance of a beating-like phenomenon. The maximum strain for this case was 2·88%.

The power spectrum in this case is also of interest, since with the broadband input spectrum, the output energies will be those not filtered by the structure. Looking at Figure 13, we find that the spectrum here is not markedly different than for the previous cases. This similarity reinforces the view of the structure as a filter, allowing oscillations at

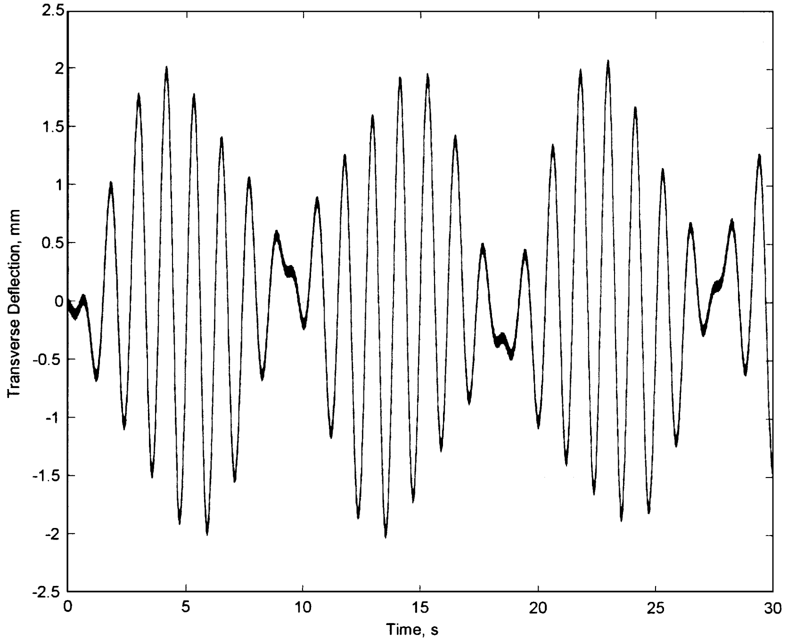

Figure 10. Response to $F_0 = 0{\cdot}003(\sin(5t) - \cos(t))$.

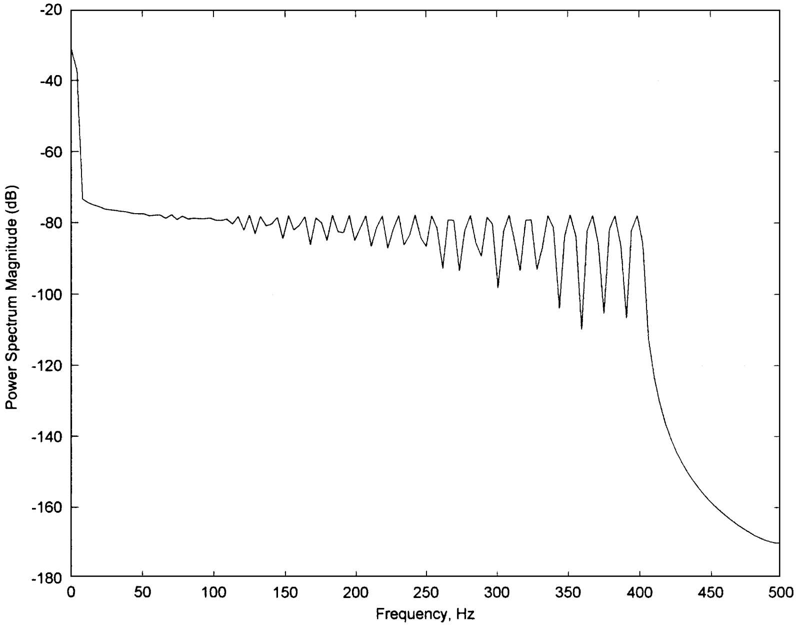

Figure 11. Power spectrum of the Fourier series input.

energies corresponding to its fundamental frequencies, in both the transverse and longitudinal directions.

Our next case is the response to this same Fourier series input forcing, except now we also introduce an initial angle of $\theta_0 = 0{\cdot}057°$. (This angle was chosen for convenience, as

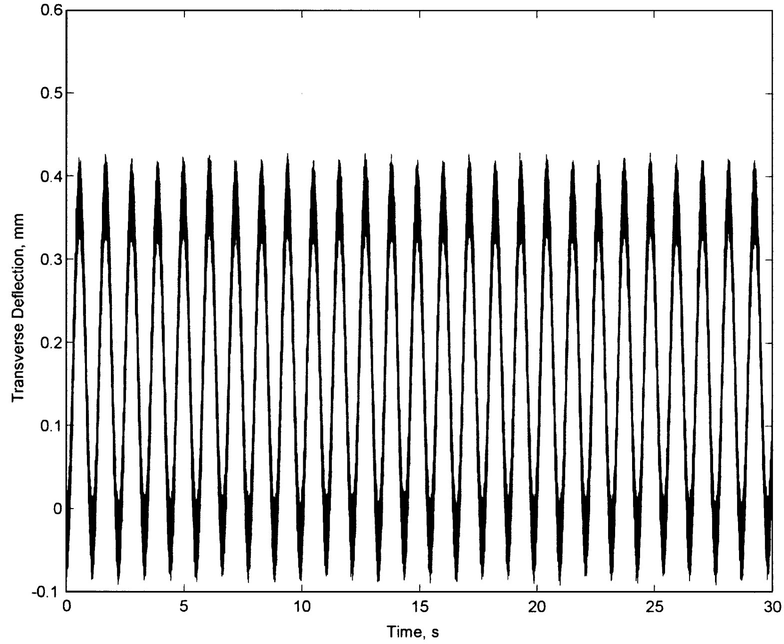

Figure 12. Transverse response to the Fourier series input $F_0 = 0{\cdot}003/\sqrt{2} + (0{\cdot}001/50)\sum_{n=0}^{50}\cos(n^2 t)$.

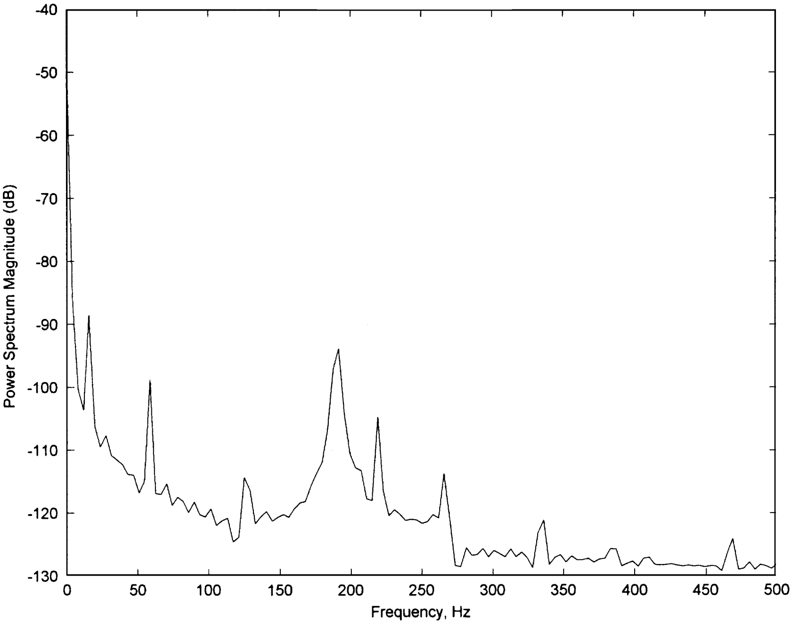

Figure 13. Power spectrum for the transverse response to the Fourier series input.

its tangent is 0·001.) Note that the initial displacement at the top of the tower (1·2 mm) is greater than the maximum displacement with zero initial conditions. The resulting motion is shown in Figure 14. The response retains the same character as with no initial displacement, except now the extreme displacements have become greater. Also, the

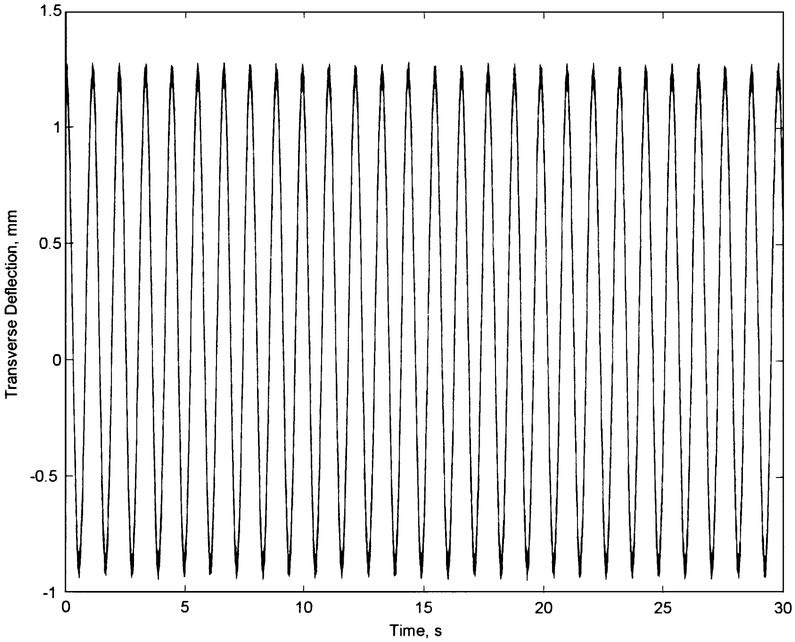

Figure 14. Response of the system to the same Fourier series input, with initial angle 0·057°.

maximum strain at the end has decreased to a value of 2·29%. The power spectrum for this simulation is virtually identical to that for the Fourier response with zero initial displacement, and thus is omitted.

Finally, we reconsider the forcing function $F_0 = 0{\cdot}003(\sin(5t) - \cos(t))$ with the same initial angle (0·057°). In this case, the initial angle gives approximately half of the maximum displacement for the time period considered with zero initial displacement. The response with a non-zero initial angle is shown in Figure 15.

Again, we see that the maximum response amplitude has increased, and that the general shape of the response is similar. The main difference between this response and that in Figure 10 is that the smaller-amplitude portions of the response (around 10 and 20 s, for example) have a larger amplitude relative to the maximum response amplitude when we include the initial angle. As with the Fourier input, the maximum strain has decreased, this time to 0·62%. Again, the power spectrum for this response is identical to that for the same system with zero initial displacement.

7.3. EXPERIMENTAL FORCING

Having tested the several cases shown above, we now move on to the external forcing found via experiment. The experimental input force is a force per unit length. Then we are able to use the Fourier series representation of the input force as the transverse force F_0, since the flexible model uses a force integrated along the length. The experimental input force is given in Figure 16 and the experimental response is plotted in Figure 17. The resulting end extension and transverse deflection are shown in Figure 18.

The analytic response shows no beating behavior. Also, the period of the analytic response is about 1·1 s, whereas the experimental response period is 1·5 s. We cannot

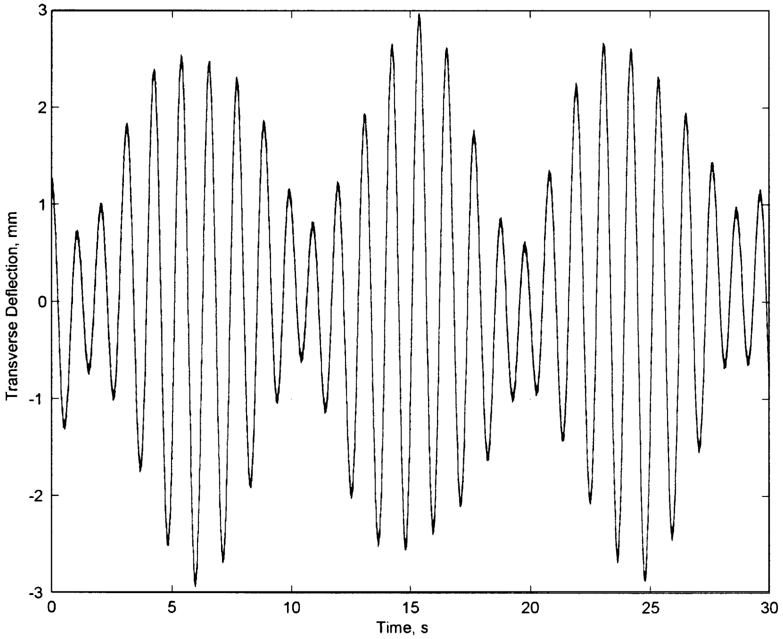

Figure 15. Transverse response of the system to $F_0 = 0{\cdot}003(\sin(5t) - \cos(t))$ and initial angle 0·057°.

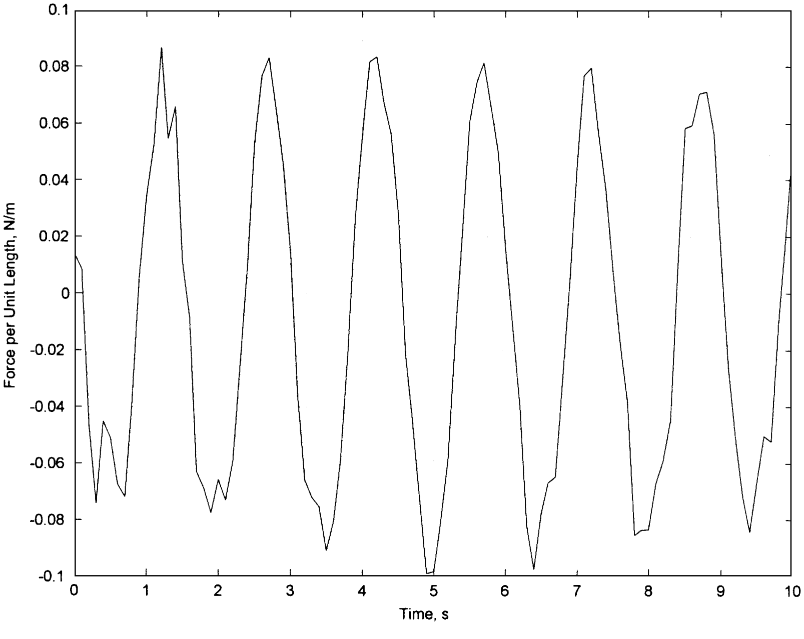

Figure 16. Input forcing from experimental data.

compare the magnitude of the response at the end to the experimentally measured response, since the laboratory apparatus measures the response at a point below the surface of the water. In our discretized tower system, the 12th node from the bottom of the tower is the closest to the point at which the response is experimentally measured.

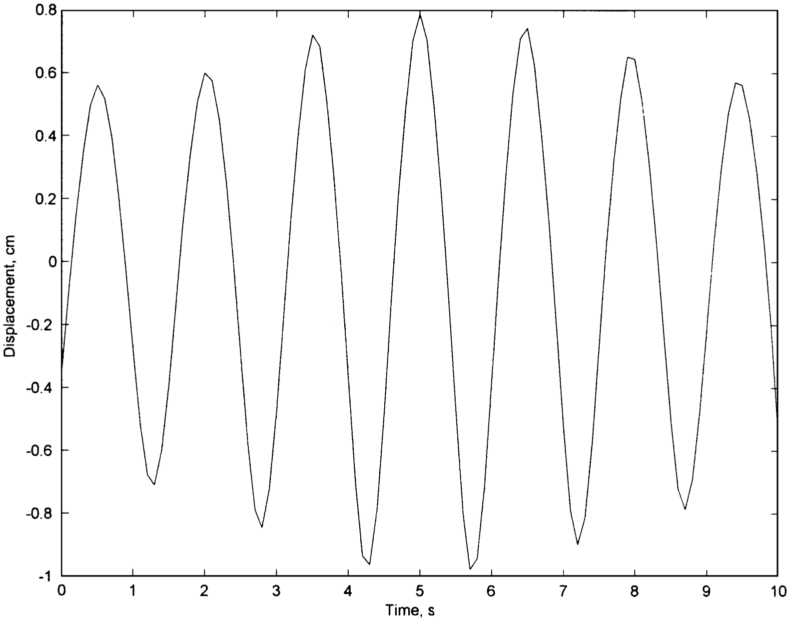

Figure 17. Experimental response to the given input dataset.

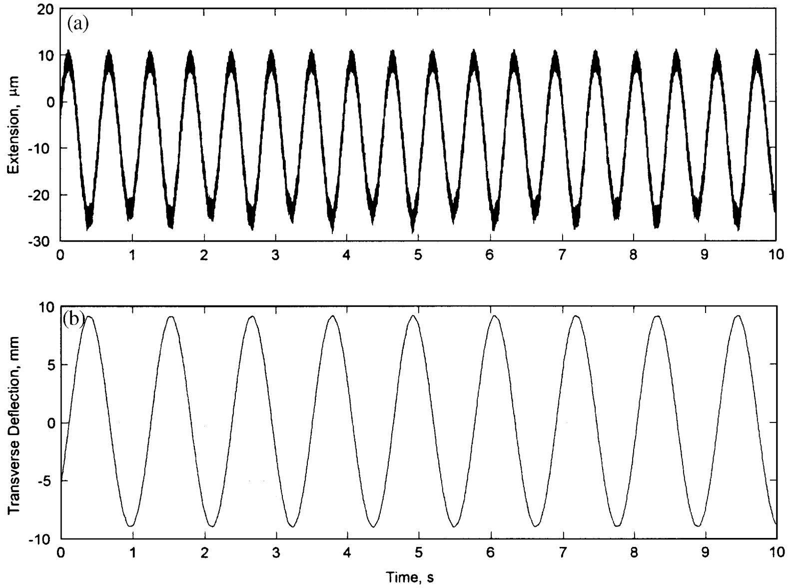

Figure 18. (a) Extensional and (b) transverse responses of the flexible model to the experimental input forcing.

Figure 19 gives the response at the closest node to the point at which the experimental data is taken. The maximum response corresponds to the minimum amplitude of beating in the experimental response. The frequency of the response also does not match the experimental data.

There are several possible reasons for the discrepancies above. The input force most likely has a three-dimensional profile, which was not reflected in the force input to the

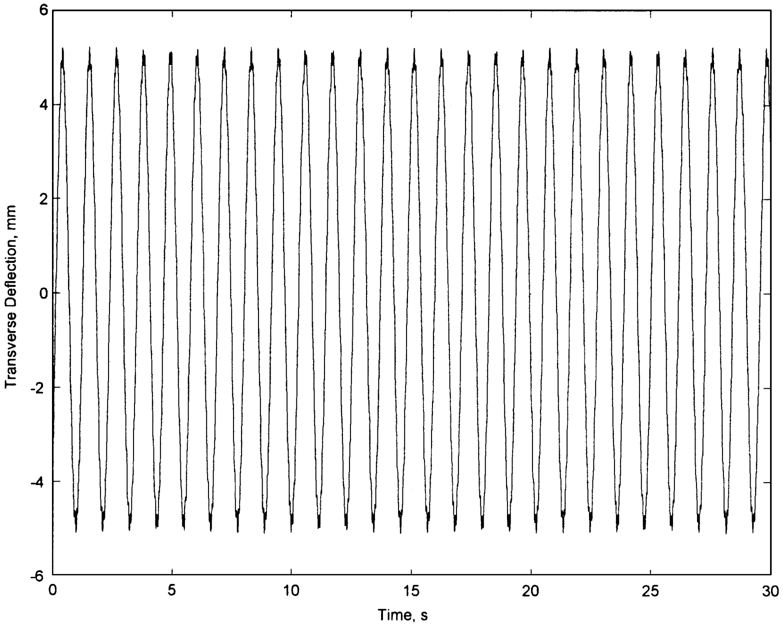

Figure 19. Response at node 12, the closest node to the point where the experimental data was taken.

model. Also, a cart/track system is used to constrain the cylinder to planar motion. This system provides damping to the cylinder by applying a force at the top end of the structure. For the discretized system modelled here, inclusion of damping is not as simple as it would be for a rigid system. Applying a damping force solely to the top node of the simulated structure has not produced satisfactory results, nor has use of a rigid-body angle and proportional damping at each node.

8. MONTE CARLO SIMULATION

The previous section introduced a model for the structure response that included bending and extensional motions. Several responses were given to different input forcing functions. The individual simulations only give a narrow sampling of the structure behavior in the presence of different inputs. Thus, to give a better idea of the overall structural behavior, we perform a Monte Carlo simulation, capturing response statistics. A discussion of random processes can be found in reference [11], and background on the Monte Carlo procedure in reference [12]. For the study at hand, it is sufficient to note that the Monte Carlo method can be broken down into three steps: simulation of the random variable, solution of the deterministic problem for a large number of random variable realizations, and statistical analysis of the results. The following sections detail these steps for our particular problem.

8.1. SELECTION OF INPUT AND OUTPUT VARIABLES

In order to perform a Monte Carlo simulation, we need to choose several input variables and their probability distributions. Then we will examine the statistics of certain parameters of the output that will help create a better picture of the overall response behavior.

There are several input parameters that we can vary. For the current study, we chose three: the maximum response amplitude, A_{max}, the number of input frequencies, N_f, and the initial angle, θ_0. We chose ranges of values for each of these parameters based on experience gained by creating the plots shown earlier, arriving at the chosen ranges in equation (41):

$$0{\cdot}001\ \mathrm{m} \leqslant A_{max} \leqslant 0{\cdot}1\ \mathrm{m}, \qquad 20 \leqslant N_f \leqslant 50, \qquad -1^\circ \leq \theta_0 \leqslant 1^\circ. \tag{41}$$

The output parameters of interest are maximum strain and maximum transverse deflection at the upper end. In a design problem, these could be the key parameters used to define the design space; the maximum strain criterion ensures that the response is elastic, and the maximum transverse deflection criterion gives a measure of crew comfort for an offshore tower for this study.[§]

8.2. INPUT DISTRIBUTIONS

The form of the distributions of the inputs needs to be determined as well. This decision is partially dictated by the software chosen for the simulation (MATLAB), since it is more convenient to use a built-in random number generator than to create one. Fortunately, MATLAB contains built-in generators for uniform and standard normal (Gaussian, $\mu = 0$, $\sigma = 1$) distributions. The uniform distribution is useful for the case where only the upper and lower bounds of the distribution are available, and the Gaussian form is worthwhile because it is representative of a broad range of physical phenomena.

The input to the uniform distribution is straightforward. The *rand* function within MATLAB generates a uniformly distributed random number between zero and one. Thus, to create a random input, the output from *rand* is multiplied by the length of the input range and added to the lower value. For example, if $r_{A,k}$ is the output from *rand* for the *k*th simulation to find the input amplitude, then

$$A_{max,k} = 0{\cdot}001\ \mathrm{m} + (0{\cdot}099\ \mathrm{m})r_{A,k}. \tag{42}$$

There are three important notes to this calculation. First, different random numbers were used for each variable during each simulation. This means that if $r_{A,k}$ is defined as above, and $r_{\theta,k}$ is the output from *rand* used to find the initial angle, $r_{A,k} \neq r_{\theta,k}$ in general. In other words, we are not necessarily taking all three random input values from the same portion of each distribution. Second, the number of input frequencies must be an integer. Thus, the result of the counterpart to equation (42) for the number of frequencies is rounded to the nearest integer. Finally, our input range for θ_0 is given in degrees, but MATLAB works in radians. A conversion must then be made at some point in the calculation.

The input form for the Gaussian distribution is slightly more complex. The Gaussian distribution within MATLAB (the *randn* command) generates a random value on a distribution with zero mean and standard deviation of one. Thus, we can use the *randn* command only if we know the mean and standard deviations for our input variables. Since we do not know those values explicitly,[¶] we need to find a way to create them. Since over 99% of the values in a Gaussian distribution are within three standard deviations (3σ) above and below the mean, we take the extreme values of the chosen ranges as three

---

[§] The usual criterion for ride comfort is low-frequency acceleration in transverse and extensional directions. We choose a somewhat simpler criterion here.

[¶] We have constructed reasonable but assumed ranges.

standard deviations from the mean.[‖] Now defining $r_{A,k}$ as the output from *randn* for the kth simulation to find the input amplitude, our formula for $A_{max,k}$ becomes

$$A_{max,k} = \mu_A + \sigma_A r_{A,k}, \tag{43}$$

where μ_A is the calculated mean of our range of A_{max} values, and σ_A is the standard deviation. The same notes apply to this calculation as the uniform calculation; that is, the random inputs are not necessarily from the same portion of the distribution, the number of input frequencies must be an integer, and the input angle must be in radians.

8.3. OUTPUT FORMS

We selected maximum strain and maximum displacement at the end of the tower as our variables of interest. Note that both of these variables will always be non-negative. Thus, we will get one-sided distributions for our variables. We will also find the mean and standard deviation for the outputs from both the uniform and Gaussian distributions. This data will allow us to make statements about the overall behavior of the system.

8.4. COMPUTATIONAL DETAIL

All that remains is to select a number of simulations and a platform upon which to run them. We wish to have our overall input distributions as close to the expected form as possible, for which more simulations is the answer. However, we also have the limitation of computational time and resources, so we arrived at 200 as a reasonable number of experiments to run. As we shall see, even though the input distributions that arose from 200 simulations were not ideal, their statistics matched well with the assumed forms.

We were able to use the Rutgers Computational Grid (RCG Cluster) to run these simulations. The RCG Cluster is a pilot program at Rutgers University, consisting of 107 Pentium II and III processors on Linux-based systems. The load sharing facility (LSF) software used on the cluster allows several batch jobs to be submitted simultaneously. Their progress can be monitored through the standard output. The batch jobs, however, do not take precedence over jobs submitted by the actual owner of the processor; the jobs submitted through LSF run when the processor in question is otherwise idle. We submitted our Monte Carlo simulations in runs of 50 simulations each, with each simulation consisting of 10 s of response time. Each batch of 50 took approximately 10 days to complete on the cluster. For comparison, a set of 10 simulations, each reflecting 10 s of response time, took about 12 h to complete on a Pentium III 533 MHz processor, with 256 Mb of RAM and running Windows 98. The difference in computational time arises because the Windows machine was dedicated solely to the Monte Carlo simulation, while the machines of the cluster were only running the Monte Carlo jobs for part of the day.

9. SIMULATION WITH GAUSSIAN INPUTS

We performed Monte Carlo simulations with both uniform and Gaussian input variable distributions. The Gaussian distributions led to better results, and thus we present only the results using Gaussian variables here.

[‖] This means the entire chosen range covers 6σ.

We begin by showing histograms of our input variable distributions for the 200 simulations performed. Figure 20 is a histogram of the force amplitudes input to the simulation. The mean amplitude is 0·0467 N/m, and the standard deviation is 0·0142 N/m. From the above, the mean of the input amplitude is 0·0505 N/m and the standard deviation 0·0165 N/m, so the data for the simulation mirrors our assumed input form for the program.

Figure 21 is the input frequency histogram of the number for the Gaussian simulation. Note that this number must be an integer. The mean of the distribution shown is 35·5, and the standard deviation 4·73. The mean used in the code was 35·0, and the standard deviation 5·0, so this distribution has similar statistics to the assumed input.

Finally, we show the distribution of initial angles in Figure 22. The mean initial angle is 0·034°, and the standard deviation 0·287°. This compares favorably to the assumed mean of 0° and standard deviation of 0·333°, in spite of the somewhat non-Gaussian behavior of the distribution around −0·2°.

With the inputs for the Gaussian simulation characterized, we move on to the output histograms. Figure 23 gives the distribution of the maximum end strains. The figure shows that 181 of the 200 runs had a maximum strain of less than 5%. However, plastic deformation was assumed to set in at 4% strain. Further examination of the data shows that 165 of the 200 simulations, or 82·5%, remain within the elastic region. The mean maximum strain is 3·6%, with a standard deviation of 4·97%. Again, to compare this distribution to a classical Gaussian distribution, we should use one-half of the calculated standard deviation as the standard deviation. By this measure, we would expect about 98% of the data to fall between zero and 8·6% strain. Examination of the data shows that 181 of the 200 simulations fall in this range, or 90·5%. So the output distribution is not Gaussian. This result is not unexpected since the system being examined is non-linear.

The other output of interest is the maximum end deflection, for which a histogram is given in Figure 24. The mean deflection is 5·6 mm, and the standard deviation is 4·1 mm.

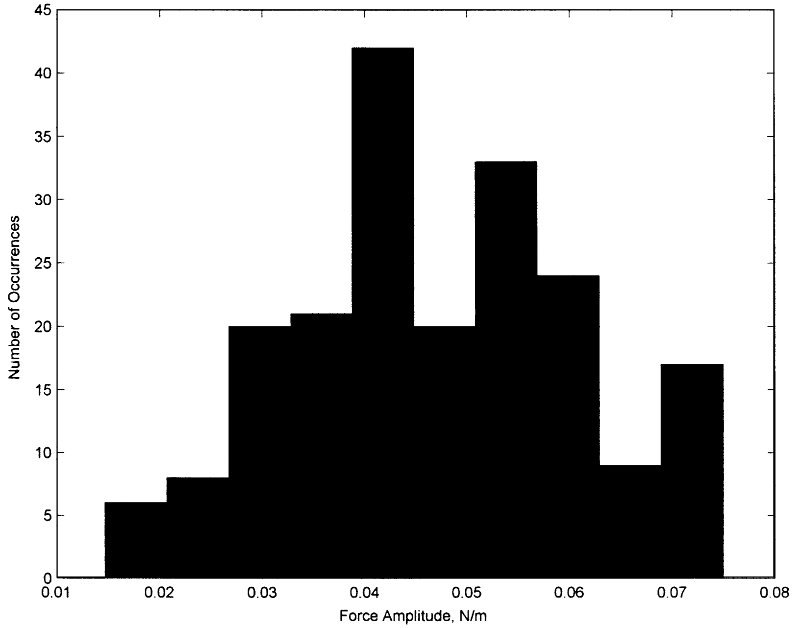

Figure 20. Force amplitude histogram for the Gaussian distribution.

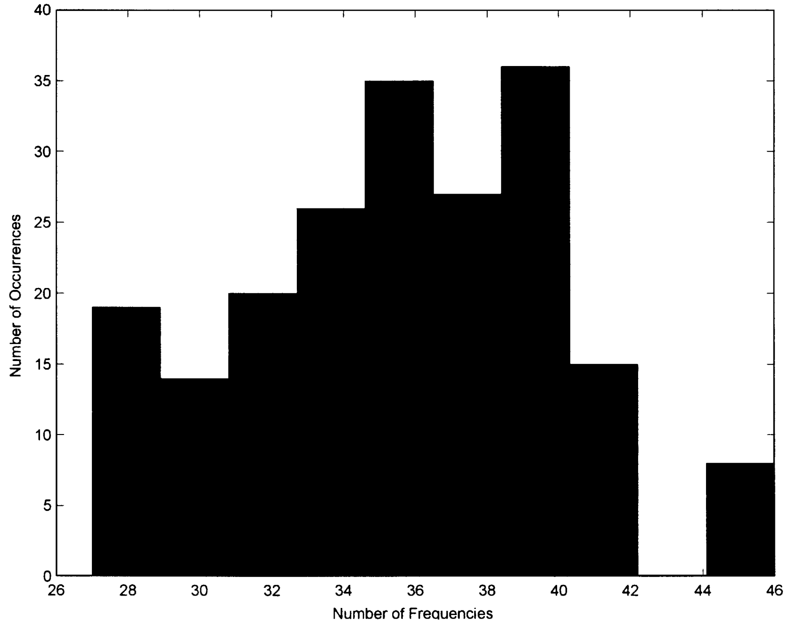

Figure 21. Histogram for the number of frequencies input to the Gaussian simulation.

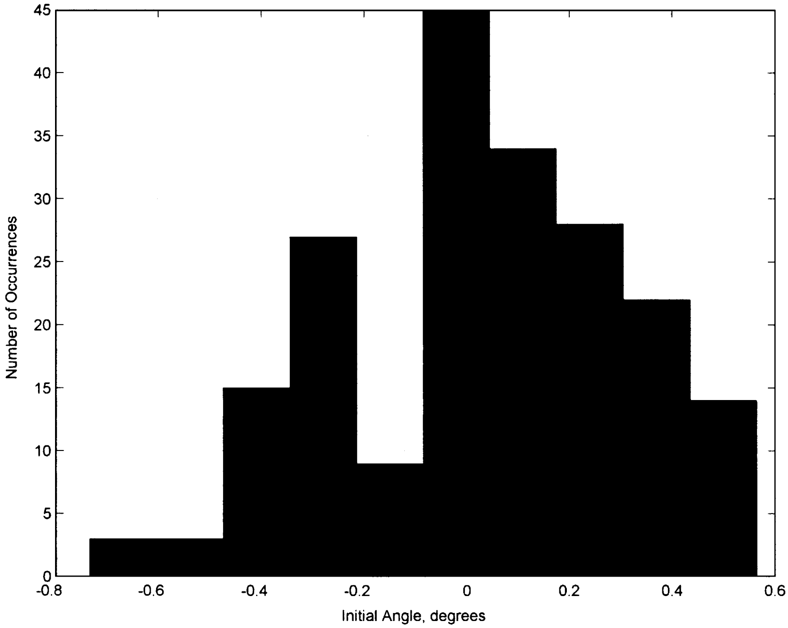

Figure 22. Histogram of input initial angles for the Gaussian Monte Carlo simulation.

Note that 174 of the 200 simulations, or 87%, have maximum deflection of 9·7 mm or less. The mean is approximately 0·004% of the tower length. Approximating scale as in the previous section, this is comparable to a maximum deflection of 1·4 m over a 350 m tower.

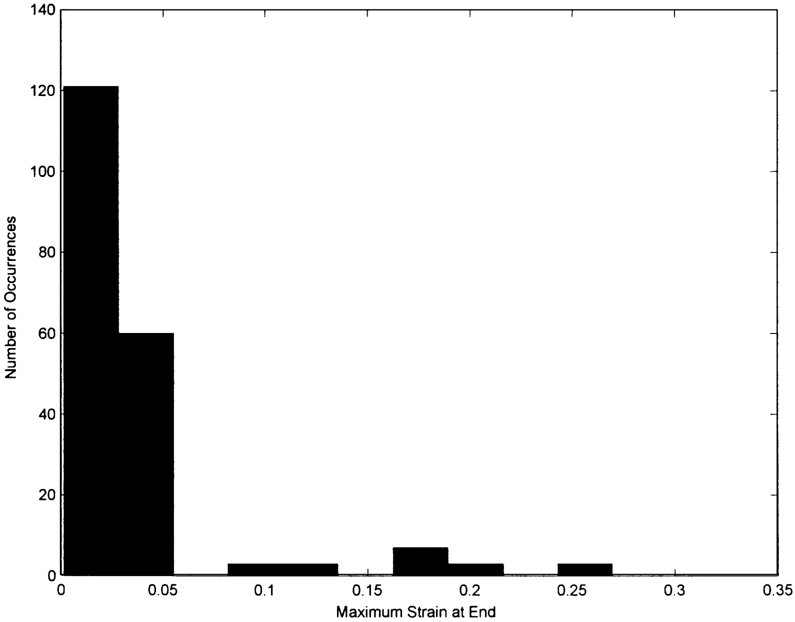

Figure 23. Histogram of the maximum end strains for the Gaussian simulations.

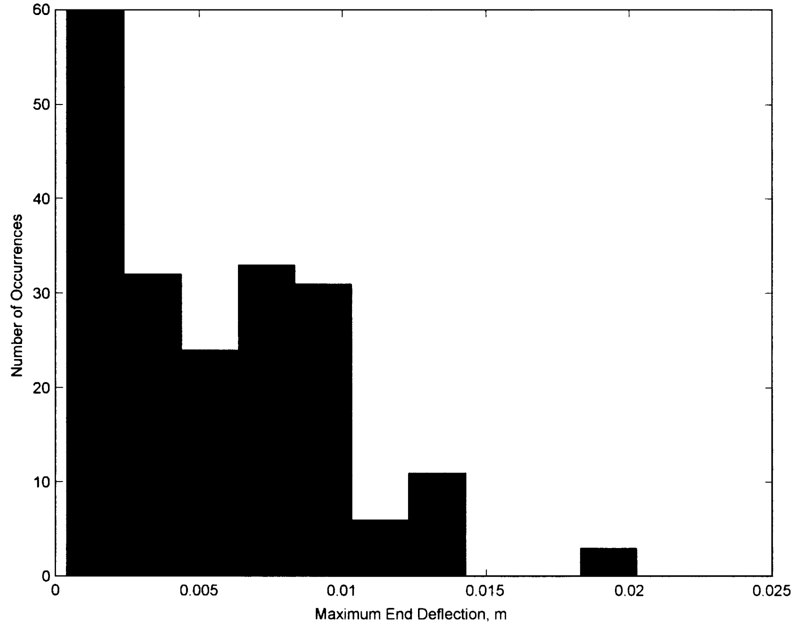

Figure 24. Histogram of the maximum end deflections for the Gaussian simulation.

10. CONCLUSIONS AND FUTURE WORK

A continuous model for a tower in water has been developed, taking into account the coupled transverse and extensional motions of the structure. Using experimental data and material properties from an experimental set-up, we have simulated several numerical solutions to the non-linear coupled equations of motion. The solutions presented here all fall within the elastic range for the material and show stable motion for the time period simulated. The power spectra from these different simulations over many forcing frequencies imply that the structure filters out energy inputs at frequencies other than its harmonics (transverse and extensional). The introduction of a non-zero initial displacement to the system causes an increase in response amplitude, but a decrease in maximum strain at the tower top and little change in the qualitative aspects of the response.

The model was tested in the presence of experimental force data. Matching between the model and observed responses needs improvement, mainly due to the presence of damping in the experimental system. An accurate method for describing the damping force applied to the model derived here will lead to a model response that better matches with experimental observation. However, we believe the modelling framework is viable for the problem under study. There are difficult issues to resolve, but they are being worked out as we gain a better understanding of the Hamilton–McIver framework.

Monte Carlo simulations were performed to test the system response to a range of inputs. The model behavior was found to be unsatisfactory for uniform inputs over the chosen variable ranges. However, the response statistics were quite good for normally distributed input variables. Since most natural processes are modelled as Gaussian distributions, the tower model shows acceptable responses to variable sets that more closely reflect those that may be encountered in nature. Also, the Monte Carlo simulation used here provides a framework for future model analysis. Changes to the cylinder model will not change the basic procedure for the Monte Carlo simulation, so the groundwork for future analyses has been laid here.

Some expansions of this model are warranted. A non-dimensional form of this model can be instructive, as its responses to different inputs may illustrate response trends in the presence of flows at different Reynolds numbers. Also, experimental data needs to be taken at more Reynolds numbers; the dataset used in this work was taken at a Reynolds number of 2440. Both of these improvements will help with scaling of the model response, possibly to the scale of offshore structures.

ACKNOWLEDGMENTS

This work is supported by the Office of Naval Research Grant No. N00014-97-1-0017. The authors are grateful for this support from ONR and program manager Dr Thomas Swean as well as for his interest in our work. The authors would also like to thank Professor Timothy Wei of Rutgers University and his experimental group for their assistance and data.

REFERENCES

1. T. Sarpkaya 1979 *Journal of Applied Mechanics* **46**, 241–256. Vortex-induced oscillations: a selective review.
2. P. Bearman 1984 *Annual Review of Fluid Mechanics* **16**, 195–222. Vortex shedding from oscillating bluff bodies.
3. K. Billah 1989 *Ph.D. Thesis*, *Princeton University*. A study of vortex-induced vibration.
4. S. Kuchnicki 2001 *Ph.D. Thesis*, *Rutgers*, *the State University of New Jersey*. Analysis of the vortex-shedding induced response of a compliant structure.
5. R. Adrezin, P. Bar-Avi and H. Benaroya 1996 *Journal of Aerospace Engineering* **9**, 114–131. Dynamic response of compliant offshore structures—review.

6. S. Han and H. Benaroya 2000 *Journal of Sound and Vibration* **237**, 837–873. Nonlinear coupled transverse and axial vibration of a compliant structure 1: formulation and free vibration.
7. S. Han and H. Benaroya 2000 *Journal of Sound and Vibration* **237**, 874–899. Nonlinear coupled transverse and axial vibration of a compliant structure 2: forced vibration.
8. D. McIver 1973 *Journal of Engineering Mechanics* **7**, 249–261. Hamilton's principle for systems of changing mass.
9. H. Benaroya and T. Wei 2000 *Journal of Sound and Vibration* **238**. Hamilton's principle for external viscous fluid structure interaction.
10. R. Adrezin 1997 *Ph.D. Thesis*, *Rutgers*, *the State University of New Jersey*. The nonlinear stochastic dynamics of tension leg platforms.
11. P. Wirsching, T. Paez and K. Ortiz 1995 *Random Vibrations*: *Theory and Practice*. New York: John Wiley and Sons, Inc.
12. I. Elishakoff 1983 *Probabilistic Methods in the Theory of Structures*. New York: John Wiley and Sons, Inc.